



# Dynamic characteristics and deterioration mechanism of coal under distinct initial gas pressure

Huaiqian Liu · Lei Wang · Hongbao Zhao · Shaobo Li

Received: 17 June 2023 / Accepted: 19 August 2023  
© The Author(s) 2023

**Abstract** Additional to dynamic and static superimposed loads, gas effects frequently affect coal seams throughout the coal mining process. It is crucial to comprehend coal samples' mechanical properties and deterioration mechanisms under distinct initial gas pressure conditions. Consequently, the dynamic compression experiment of coal samples was conducted utilizing a self-developed observable combined dynamic and static loading test system of gas-bearing coal (GAS). The mechanical characteristics including failure mode in coal samples under distinct initial gas pressures were studied. Furthermore, the mechanism of gas deteriorated mechanical parameters and aggravated the propagation of cracks when combined with dynamic and static loads was revealed. The conclusions are drawn as follows: The GAS can go through four stages of deformation: elastic stage, elastoplastic stage, plastic stage, and failure stage. Furthermore, the dynamic strength and failure strain deteriorated with increasing gas pressure. Based on computed tomography (CT) technology, it is found that the

splitting-spallation composite cracks of impacted samples become more noticeable with rising initial gas pressure, and finally, the two kinds of cracks create a complex reticular crack system. Meanwhile, the crack volume and fractal dimension increase with rising gas pressure, indicating that gas can aggravate the coal's failure degree. Under combined dynamic and static loads, the deterioration model of mechanical parameters of GAS is obtained, that is, with rising initial gas pressure, the dynamic strength of coal samples reduces and the failure strain rises synchronously. The main reason for the aggravation of compound failure in impacted samples is that the stress intensity factor rises with the rise of gas pressure. These conclusions enrich the basic theories such as the inducing mechanism of dynamic disasters caused by coal-rock-gas compounds and can offer a theoretical foundation for the technology employed in monitoring, early warning, and prevention of dynamic disasters in compounds.

## Article Highlights

1. The dynamic characteristics under different initial gas pressures were studied by the self-developed observable combined dynamic and static loading test system of gas-bearing coal.
2. Based on computed tomography technology, it is found that the splitting-spallation composite cracks of impacted samples become more noticeable with rising initial gas pressure.

H. Liu · L. Wang (✉) · H. Zhao · S. Li  
State Key Laboratory of Mine Response and Disaster Prevention and Control in Deep Coal Mine, Anhui University of Science and Technology, Huainan 232001, China  
e-mail: 343002964@qq.com; leiwang723@126.com

H. Liu · H. Zhao  
School of Energy and Mining Engineering, China University of Mining and Technology (Beijing), Beijing 100083, China

3. The mechanism of gas deteriorates dynamic mechanical parameters, and aggravates coal samples' failure under the combined dynamic and static loading are revealed.

**Keywords** Combined dynamic and static loading · Gas-bearing coal · Mechanical characteristics · Deterioration mechanism

## 1 Introduction

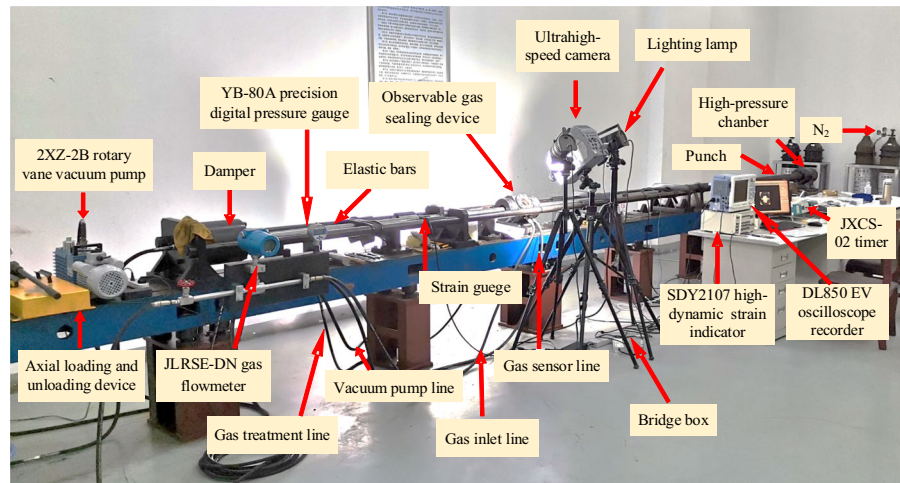
Currently, the dynamic load derived from mining disturbances including the breaking of the roof, activation of fault, or blasting operations affects the coal seams in addition to being impacted by the ground stress during the coal mining process (Ai et al. 2019; Yin et al. 2020; Kong et al. 2021). The depletion of shallow resources also causes coal mining to reach depths of 10 to 25 m/a (Zhao et al. 2020; Yuan 2021). As coal seams are mined deeper, their gas pressure and content increase as well. This causes substantial variations in the mesoscale damage as well as macroscale failure between GAS seams and gas-free coal seams during impact loads and even lowers the coal seams' critical failure index (Kong et al. 2020). Thus, studying the dynamic characteristics including failure mode in coal samples under distinct gas pressure, and revealing the deterioration mechanism of GAS under the combined dynamic and static loads are particularly important to enrich the mechanism of the dynamic disaster in the coal-rock-gas compound.

Numerous investigations exist on the mechanical characteristics of GAS: Bieniawski et al. (1968), Ates et al. (1988), Medhurst et al. (1997), and Viete et al. (2006) concluded that the coal's compressive strength and elastic modulus may deteriorate owing to adsorption of gas. Ranjith et al. (2010) and Xie et al. (2014, 2015, 2017) found that coal is prone to expansion deformation with rising gas pressure, and the failure form aggravates. Similarly, Wang et al. (2021a) obtained that the crack volume rises with rising gas pressure, and the distribution characteristics are more complex by three-dimensional reconstruction. The studies mentioned above primarily focus on the static characteristics of GAS. Nevertheless, the dynamic load generated by occurrences like roof fracture and fault activation is present during the coal seam mining

process. Consequently, employing a split Hopkinson pressure bar (SHPB), several researchers have started studying the dynamic characteristics of coal and rock. Han et al. (2020) examined the dynamic characteristics of joint sandstone filled with layers of various thicknesses and discovered that as joint thickness increased, both the energy absorption and dynamic strength decreased. Klepacko et al. (1984) found that the elastic modulus and crack growth rate of coal are very sensitive to strain rate based on the SHPB system. Zhang et al. (2019) concluded that the coal's dynamic failure process can be split into the initial nonlinear stage, yield stage, stress strengthening stage, and unloading failure stage. In their study of the impacts of static axial prestress on the Brazilian coal disc sample's dynamic tensile strength, Hao et al. (2020) discovered that when static axial prestress increases, the dynamic tensile strength initially rises and then falls. Li et al. (2005) established a combined dynamic and static loading constitutive model combined with statistical damage and a viscoelastic model, which essentially explained the dynamic characteristics of coal and rock. Utilizing the elastic-plastic theory, the damage-viscoelastic constitutive model was constructed by Fu et al. (2013). In summary, the research mentioned above primarily concentrates on the static characteristics of GAS or the dynamic behaviors of coal and rock, whereas it is needed to improve and enrich the mechanical characteristics of GAS under combined dynamic and static loading.

The studies show that coal will be deteriorated due to the gas erosion effect (He et al. 1996). There are many methods to quantify the deterioration trend or failure degree of materials: the ratio of elastic modulus after deterioration to initial elastic modulus is defined as a damage variable in the equivalent strain hypothesis (Lemaitre 1984). Wang et al. (2021b) measured the deterioration of coal by analyzing the change of uniaxial compressive strength under different initial gas pressure. Barile et al. (2019) and Liu et al. (2009) based on an acoustic emission technique to measure the damage degree of material. Ma et al. (2019) and Ma et al. (2020) defined the ratio of dissipation energy to total input energy before peak strength as a coal-rock damage variable. Xu et al. (2010) and Liu et al. (2019) used wave velocity to quantify the deterioration of the rock under cyclic impact. Jin et al. (2011) defined the rock damage degree based on wave impedance.

**Fig. 1** Observable combined dynamic and static loading test system of GAS



Meanwhile, some scholars define damage degree by analyzing the changes in the area or length of the crack in a two-dimensional plane (Chen et al. 2005; Ge et al. 1999). The studies mentioned above are mainly based on the loss of mechanical parameters or change of plane geometry shape to measure the damage degree. However, the material deterioration originates from crack initiation and propagation in the microelement. In particular, as a dual medium (Thararoop et al. 2012), gas underloading can cause the gas–solid coupling effect to occur with coal (Xie et al. 2014, 2017), which further aggravates the failure. Therefore, the anisotropic deterioration or failure measured by the three-dimensional (3D) crack in coal samples needs to be further studied. Moreover, the deterioration mechanism of GAS under the combined dynamic and static loading also needs to be revealed.

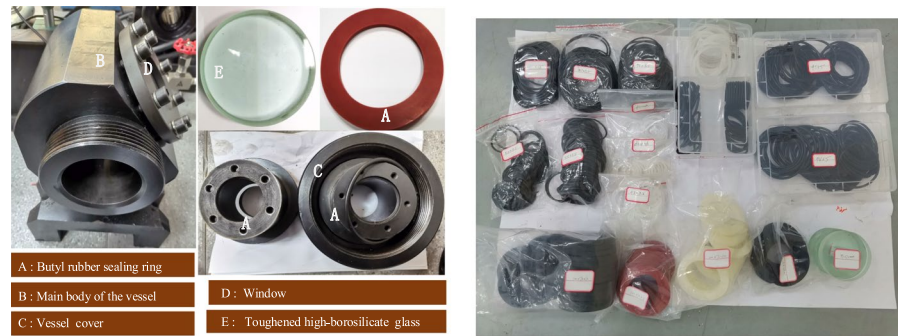
In light of this, this research develops a set of observable combined dynamic and static loading test systems for GAS. The dynamic characteristics of GAS are examined after a dynamic compression experiment is conducted with distinct initial gas pressure. Moreover, on the basis of CT technology, the crack volume and fractal dimension of coal samples under distinct initial gas pressure are quantitatively characterized, and the mechanism of gas-deteriorated mechanical parameters and aggravated propagation of cracks of coal samples under the combined dynamic and static loading is discovered. These findings can serve as the theoretical foundation for the technology used in monitoring and early

warning of the dynamic disaster in coal-rock-gas compounds in coal mine subject to impact load.

## 2 Observable combined dynamic and static loading test system of GAS

### 2.1 The test system's technical index and applicability

The observable combined dynamic and static loading test system of GAS (Fig. 1) is effectively enhanced by utilizing a one-dimensional combined dynamic and static loading test system, and the test system's theoretical feasibility is confirmed (Liu et al. 2023). A dynamic and static load application device, a device for gas supplying/exhausting and monitoring, a device for strain acquisition, and a device for the acquisition of digital images are the major components of the test system. A damper, a timer, elastic bars, an axial loading/unloading device, a cylindrical punch, and a high-pressure chamber make up the load application device. 40 Cr alloy steel was utilized for making all of the punch and elastic bars, which has a density of  $7796 \text{ kg/m}^3$ , a Poisson's ratio of 0.30, a wave velocity of 5190 m/s, and an elastic modulus of 210 GPa. The elastic bars' punch, incident, transmitted, and absorption bars are each 50 mm in diameter, and their lengths are 300, 2000, 1500 and 500 mm, respectively. An observable gas sealing device, a JLRSE-DN gas flowmeter, a YB-80A precision digital pressure gauge, and a 2XZ-2B rotary vane vacuum pump make up the device for the purpose of gas

**Fig. 2** Observable gas sealing device and Sealing rings

(a) Observable gas sealing device

(b) Sealing rings of different materials and sizes

supplying/exhausting and monitoring. The toughened high-borosilicate glass used in gas sealing devices has a maximum yield strength of 20 MPa, the size is 95 mm in diameter  $\times$  20 mm in thickness. The digital pressure gauge's measurable range is between -0.1 and 3.0 MPa, and  $10^{-4}$  is the acquisition accuracy in real time. The pump's maximum vacuum capacity reach to 6.0 MPa. The DL850EV oscillograph recorder, BX120-2AA strain gauge, SDY2107A high-dynamic-strain indicator, and bridge box make up the strain acquisition device. The oscillograph recorder can sample at a rate of up to 100 MS/s. In this experiment, the sampling velocity of oscillograph recorder is set to 10 MS/s, the recording length is 10 K, which can satisfy the data acquisition needs. The illumination lamp, ultrahigh-speed camera and synchronous trigger device make up the digital image acquisition system. The  $1024 \times 1024$  pixels is the maximum image resolution,  $10^5$  fps is the maximum frame rate.

## 2.2 Adjustment and testing of system gas tightness

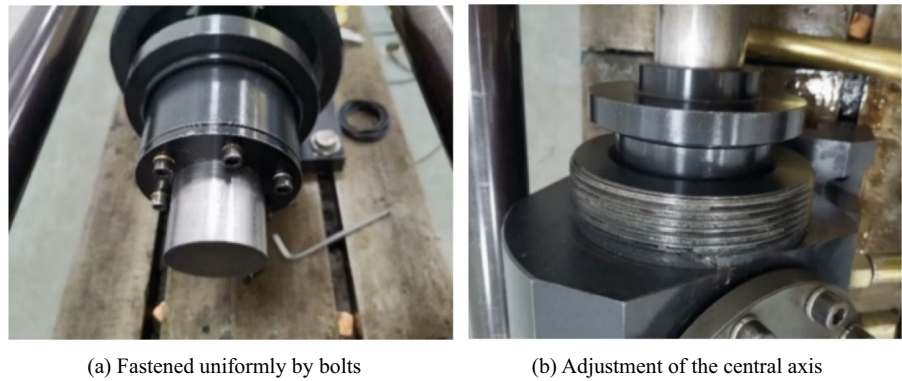
As shown in Figs. 1 and 2a, the observable gas sealing device is made up of sealing rings, vessel cover, window, the vessel's main body, toughened high-borosilicate glass, vacuum pump line, gas inlet line, gas sensor line, and gas treatment line. For combined dynamic and static loading testing of GAS to be successful, an observable gas-sealing device must be gas-tight. Therefore, the sealing rings of different materials and sizes are compared comprehensively (Fig. 2b). Finally, a 95 mm outer diameter  $\times$  5.7 mm thickness butyl rubber sealing ring was utilized to join the ends of the gas vessel's main body and gas vessel cover in order to confirm gas tightness during the process of impact loading and adsorption of gas.

The 48 mm outer diameter  $\times$  3.5 mm thickness butyl rubber sealing ring secured the gas vessel cover to the incident bar and the transmission bar. A 100 mm outer diameter  $\times$  70 mm inner diameter  $\times$  10 mm thickness butyl rubber gasket was utilized to seal the window and toughened high-borosilicate glass.

The system's installation and adjustment steps of the gas tightness are as follows: First, bolts were used to consistently secure the position of the gas vessel cover to the elastic bar, the gas vessel's main body, and the connection between the sealed vessel's main body and the window, in case the unequal force resulted in inadequate sealing. Second, the coal was positioned between the incident bar and the transmitted bar with a Vaseline applied to both ends and clamped to avert the coal from tumbling off using the axial loading and unloading device with the elastic bar and the central axis of the main body of the gas sealed vessel in alignment. Figure 3 depicts the installation process in order. Third, after closing the valves on the gas inlet and gas treatment lines, the vacuum pump's valve was opened and vacuumed for 3 min until the gas pressure stabilized at -0.1 MPa. Then, the vacuum pump's valve was shut. Lastly, the inlet valve and high-pressure gas cylinder were opened, and the observable gas sealing device was filled with gas. The inlet line and high-pressure cylinder valves were shut to perform the coal sample's gas adsorption operation when the predetermined gas pressure value was reached. Particularly,  $\text{CH}_4$  made about 83–89% of the total gas in the coal mine, making it the major gas component. Thus,  $\text{CH}_4$  was selected as the experimental gas, also known as the gas in this work.

The initial gas pressures evaluated varied from 0 to 2.0 MPa, at an interval of 0.5 MPa, and an adsorption time of 12 h was employed to test the gas tightness of

**Fig. 3** Installation step of the gas sealing device



(a) Fastened uniformly by bolts

(b) Adjustment of the central axis

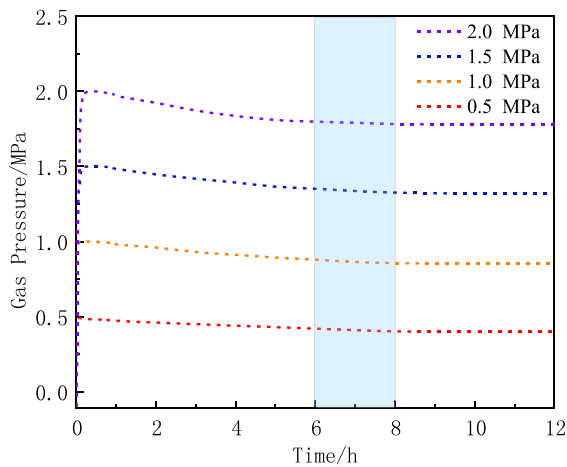


**Fig. 4** Variation trend of gas pressure

the observed gas sealing device. The observable gas sealing device's change in gas pressure is depicted in Fig. 4: the gas pressure increases quickly, declines quickly, declines slowly, and then remains practically constant. The following is an explanation of how gas pressure changes: First, the gas pressure rises quickly as the gas spreads quickly throughout the vessel after being introduced into a gas sealing device in accordance with the predetermined value. Second, the gas inlet valve is shut when the gas pressure reaches the predetermined value. Because coal is a dual medium, fast-filling of pores and cracks are caused by the free gas, causing the gas pressure in the sealed vessel to drop quickly. Third, Van der Waals forces cause the free gas to change into the adsorption state on the surface of the pores and cracks once it has filled the coal's pores and cracks, and the adsorbed gas no longer transfers gas pressure (Li et al. 2015), which



**Fig. 5** Coal samples

causes the gas pressure in the gas sealing device to further decline. Once the adsorbed gas reaches saturation, the free gas pressure becomes practically stable. Therefore, it can be inferred that the gas sealing device has respectable gas tightness and satisfies the experimental requirements.

### 3 Experimental methods

#### 3.1 Sample preparation

First, for the purpose of reducing the experimental error due to the bedding direction, the inertial effect, and end-face friction (Lu et al. 2013), following ISRM regulations, coal with vertical bedding was sampled by a sampler, and standard cylindrical coal samples with a diameter of 50 mm and a height of 30 mm were prepared by a cutting mill. For coal samples, the nonparallelism had to be less than 0.02 mm and the unevenness had to be less than 0.05 mm on both ends (Fig. 5). Second, the coal samples' wave velocity ( $c_s$ ), size, and quality were precisely

determined to decrease the inaccuracy triggered by the coal's discreteness. Coal samples that deviated 10% from the average wave velocity were eliminated (Jiao et al. 2021; Yuan et al. 2021). Lastly, using CT technology, the scanning and reconstruction of coal samples were performed, and the samples that had thoroughgoing cracks or noticeable sections were deleted, as shown in Fig. 6. This further reduced the impact of cracks and joints on the findings of experiments. At a target gas pressure, there are three coal samples for each series of testing, and Table 1 lists their physical properties.

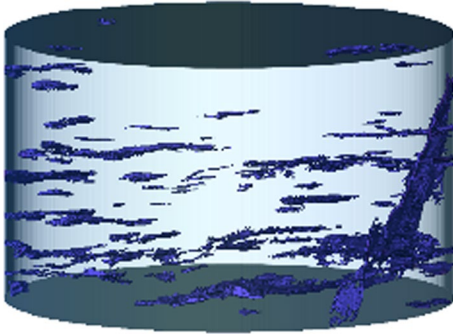


**Fig. 6** Coal with throughgoing crack

**Table 1** Physical and mechanical properties of coal samples

No	Density ( $\text{g}/\text{cm}^3$ )	$c_s$ ( $\text{m}/\text{s}$ )	Gas pressure ( $\text{MPa}$ )	$\sigma_d$ ( $\text{MPa}$ )	Average $\sigma_d$ ( $\text{MPa}$ )	$\varepsilon_{peak}/10^{-3}$	Average $\varepsilon_{peak}$	DIF	Average DIF
G-0-1	1.28	1123	0	41.65	42.70	9.21	9.35	1.72	1.77
G-0-2	1.29	1187		43.75		9.36		1.81	
G-0-3	1.30	1103		42.70		9.47		1.77	
G-0.5-1	1.30	1132	0.5	37.82	37.66	10.09	10.03	1.79	1.79
G-0.5-2	1.31	1168		38.05		10.04		1.81	
G-0.5-3	1.29	1063		37.10		9.96		1.76	
G-1.0-1	1.32	1129	1.0	35.70	36.03	10.22	10.18	1.88	1.90
G-1.0-2	1.30	1049		36.40		10.19		1.92	
G-1.0-3	1.33	1034		35.98		10.14		1.89	
G-1.5-1	1.30	1119	1.5	31.50	31.25	10.47	10.39	1.95	1.93
G-1.5-2	1.31	1068		32.55		10.26		2.01	
G-1.5-3	1.32	1112		29.71		10.43		1.84	
G-2.0-1	1.29	1098	2.0	26.95	26.94	11.14	11.00	1.94	1.94
G-2.0-2	1.30	1119		26.57		10.80		1.92	
G-2.0-3	1.31	1098		27.30		11.07		1.97	

**Table 2** Uniaxial compressive strength

Gas Pressure ( $\text{MPa}$ )	$\sigma_c$ ( $\text{MPa}$ )			Average $\sigma_c$ ( $\text{MPa}$ )
	1#	2#	3#	
0	24.1	23.6	24.8	24.17
0.5	20.3	21.6	21.3	21.07
1.0	18.9	19.6	18.5	19.00
1.5	16.8	16.3	15.4	16.17
2.0	14.1	13.8	13.7	13.87

### 3.2 Experimental scheme

First, using the gas–solid coupling test system, uniaxial compression experiments were conducted to offer a theoretical foundation for the GAS's impact experimentation (Xie et al. 2015), and the coal samples' uniaxial compressive strengths ( $\sigma_c$ ) under distinct initial gas pressures were found (Table 2). Second, cylindrical samples were firmly wrapped in a self-adhesive permeable bandage to keep the debris from sliding off when the coal is impacted, and coal samples were then positioned between the transmitted bar and the incident bar. Third, 3 MPa were chosen as the axial load, and the coal samples were impacted after being adsorbed for 12 h at pressures of 0, 0.5, 1, 1.5, and 2.0 MPa gas pressure, respectively. To guarantee that coal samples remained a continuous medium



**Fig. 7** Permeable bandage and impacted sample

during varied initial gas pressures, a 0.4 MPa impact pressure was chosen based on the coal samples' fragmentation state, as illustrated in Fig. 7. Vaseline was also applied to both ends of the samples as a coupling agent before to each impact experiment, and silicone rubber with dimensions of length, width, and thickness equal to 12 mm, 12 mm, and 3 mm, respectively, was employed as the wave shaper to further attenuate the effects of the dispersion effect and end-face friction (Wang et al. 2022; Jiao et al. 2021; Yuan et al. 2021).

## 4 Experimental results

### 4.1 Effectiveness analysis of experiment

Figure 8a shows the typical stress wave of coal samples under distinct initial gas pressure. However, it is challenging to maintain a constant strain rate during impact loading of coal, soft rock, and jointed rock (Han et al. 2020; Hao et al. 2020; Jiao et al. 2021; Yang et al. 2021). The average strain rate corresponding to the peak stress is used to express the coal's strain rate (T/CSRME 001-2019). In addition, the validity of the experimental data is determined by the stress balance state of samples. Therefore, taking the stress balance of the sample G-1.0-3's as an example (Fig. 8b), the reflected wave's initial voltage is not 0 because of the axial load (the corresponding time is 538  $\mu$ s), the transmitted stress prior to failure is about equal to the total of incident stress and reflected stress, and less than 5% is the stress equilibrium coefficient ( $\eta$ ) (Li 2014); that is, the stress equilibrium state has been attained in the coal sample. The coal samples that do not reach the stress

equilibrium are eliminated in the whole experimental process, and corresponding supplementary experiments are added.

### 4.2 Stress–strain characteristics

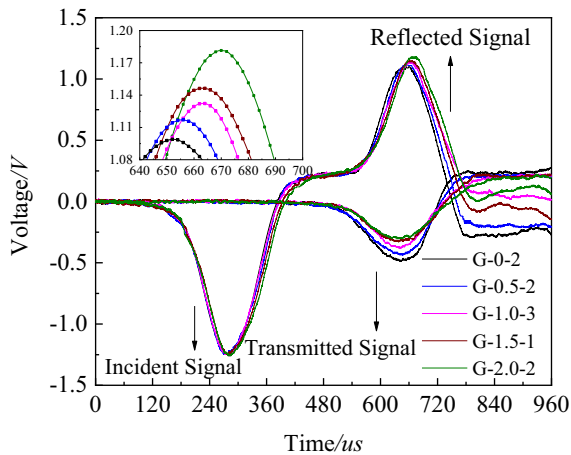
The typical coal samples' stress–strain curve depicted in Fig. 9 can be calculated using Eq. (1) as per the one-dimensional stress wave theory (Li et al. 2008).

$$\begin{cases} \sigma(t) = \frac{A_b E_b}{A_s} \varepsilon_r(t) \\ \varepsilon(t) = -\frac{2c_b}{l_s} \int_0^t \varepsilon_r(t) dt \end{cases} \quad (1)$$

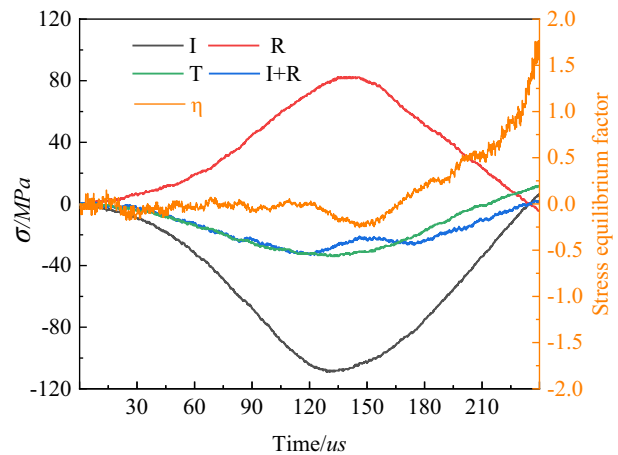
where the coal's stress, strain, sectional area and height are denoted by  $\sigma(t)$ ,  $\varepsilon(t)$ ,  $A_s$  and  $l_s$ , respectively; the section area and elastic modulus of the bar are denoted by  $A_b$  and  $E_b$ , respectively; the strain of the transmitted bar and reflected bar at the corresponding times are denoted by  $\varepsilon_t(t)$  and  $\varepsilon_r(t)$ , respectively.

The coal sample's pores and cracks are precompact by the axial load and the dynamic load immediately impacts—which causes the dynamic stress–strain curve of GAS to reach the linear elastic stage without any visible compaction stage as opposed to the static stress–strain curve. Subsequently, the elastoplastic stage is present in the coal sample, where new cracks undergo initiation and continual propagation. The stress–strain curve slowly steepens when the stress is around 80% of its maximum strength, at which point the coal sample enters the plastic stage and develops numerous little thoroughgoing cracks. Lastly, the sample is penetrated by a high number of cracks, leading to the failure stage.

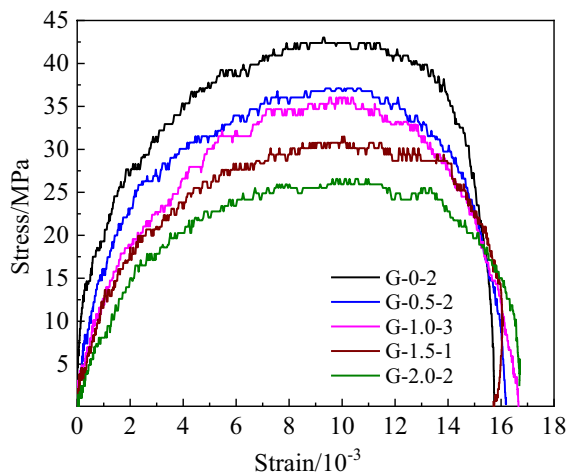
Table 1 displays the coal samples' dynamic mechanical parameters during distinct initial gas pressures. It was discovered that the coal samples' average dynamic compressive strength decreased from 42.70 to 26.94 MPa with rising gas pressure, with respective declines of 11.80%, 15.62%, 26.81%, and 36.91% when compared to the value with no gas pressure. In accordance with the failure strain, it can be expressed that the coal samples' average failure strain rises from  $\varepsilon_{peak} = 9.35 \times 10^{-3}$  under 0 MPa gas pressure to  $\varepsilon_{peak} = 11.00 \times 10^{-3}$  under 2.0 MPa gas pressure, which the rise of coal samples contrasted to that under no gas pressure is 7.27%, 8.88%, 11.12%,



(a) Typical stress wave of coal samples



(b) Stress equilibrium of the sample G-1.0-3

**Fig. 8** Verification of stress equilibrium**Fig. 9** Stress–strain curve of typical samples

and 17.65%, respectively. Numerous investigations have demonstrated that coal and rock typically have dynamic compressive strength ( $\sigma_d$ ) greater contrasted to static compressive strength ( $\sigma_c$ ). For the comparison of the coal samples'  $\sigma_d$  with  $\sigma_c$  during distinct initial gas pressures, the dynamic increase factor ( $DIF = \sigma_d / \sigma_c$  (Wang et al. 2018; Hao et al. 2012)) was utilized for measuring the strength sensitivity under two distinct modes of loading. Table 1 depicts that the coal samples' DIF rises with rising initial gas pressure, demonstrating that the reducing trend of  $\sigma_c$  is lesser contrasted to that of  $\sigma_d$  under each gas pressure;

that is, the coal samples'  $\sigma_d$  has a higher sensitivity to gas pressure.

#### 4.3 Failure mode

In view of the upward or downward trend of dynamic mechanical parameters of coal samples under gas occurrence, many scholars call it erosion or deterioration effect (He et al. 1996; Wang et al. 2021b). Nevertheless, the loss essence of the mechanical parameter is derived from the initiation, and propagation of the crack on the mesoscale. That is to say, it is crucial to reveal the deterioration mechanism of coal to characterize the crack distribution of impacted coal under distinct initial gas pressure. Therefore, the CT technology was utilized to elaborate the crack distribution characteristics, and the degree of crack propagation was quantitatively analyzed under different initial gas pressure based on the fractal theory.

##### 4.3.1 Crack distribution of slice in different layers

The layers of slice in coal samples are shown in Fig. 10, and the spacing of each slice is set to 5 mm. Table 3 shows the crack distribution of different layers after binarization. It is evident that when there is no gas pressure, several radial cracks appear inside the sample. When the initial gas pressure is 0.5 MPa, the radial crack continues to extend, and slices are divided into several areas of unequal size, finally, a



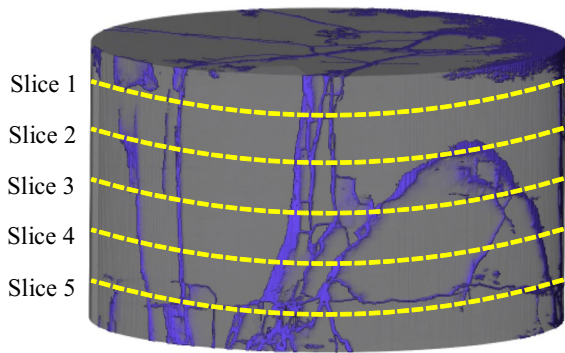


**Fig. 10** Slice location

network of reticular cracks is formed. When the initial pressure rises from 1.0 to 1.5 MPa, the reticular cracks in the sample are more developed, and even annular parallel cracks are formed. When the initial gas pressure is set to 2.0 MPa, the number of cracks rises sharply, and the fracture intensifies until the network topology of the crack is formed.

*4.3.2 Three-dimensional crack distribution of coal*

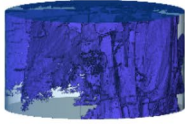
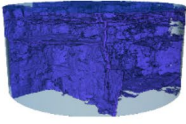


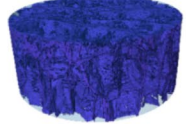
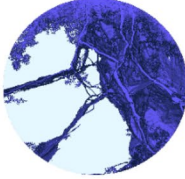
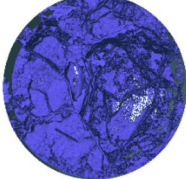
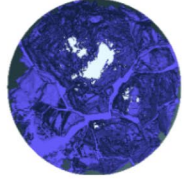
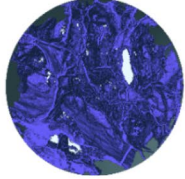
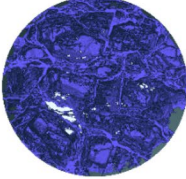
The slices can only show the local crack propagation, while 3D reconstruction can directly characterize and quantify the global crack volume and distribution

**Table 3** Crack distribution

No.	G-0-2	G-0.5-2	G-1.0-3	G-1.5-1	G-2.0-2
Slice 1					
Slice 2					
Slice layer Slice 3					
Slice 4					
Slice 5					

The black of the slice after binarization represents the crack structure

**Table 4** Three-dimensional crack fractal characteristics

No.	G-0-2	G-0.5-2	G-1.0-3	G-1.5-1	G-2.0-2
Front view					
Top view					
$V_F/cm^3$	3.78	4.17	4.46	4.78	5.02
$D_V$	2.13	2.24	2.30	2.46	2.53

The purple in the picture is a crack structure.  $V_F$  is crack volume

characteristics. Table 4 depicts the top view and front view of the crack in the impacted samples.

When there is no gas pressure acting on the impact coal sample, the sample contains axial splitting/thoroughgoing cracks triggered by the Poisson effect and a few annular cracks, and the sample shows splitting failure. When the initial gas pressure is from 0.5 to 1.0 MPa, a network of axial reticular cracks and even annular parallel cracks that converge through the section of the coal is developed. When the initial gas pressure is from 1.5 to 2.0 MPa, the axial and annular parallel cracks in the impacted sample become more prominent with rising initial gas pressure, and finally, the two kinds of cracks form a spatial reticular crack system.

The crack volume and its fractal dimension can efficiently reflect the internal failure degree of the coal sample (Fu et al. 2020). Therefore, after extracting the crack of the coal sample by 3D reconstruction technology, the complexity of cracks is quantified based on the box dimension method in the fractal theory. The method can be defined as cubes with  $\delta$  length covering the entire crack

(regardless of the boundary effect), and then the number of cubes required to fill the whole crack space is counted. Finally, the coal sample crack's fractal dimension is represented by the slope of the fitting curve (Liu et al. 2022; Wang et al. 2021a), that is:

$$D_V = -\frac{\lg N(\delta)}{\lg(\delta)} \quad (2)$$

In the formula,  $N(\delta)$  represents the number of cubes, and  $D_V$  represents the fractal dimension.

The crack volume and fractal dimension of coal samples as depicted in Table 4. It is evident that the coal samples'  $V_F$  rises from 3.78 to 5.02 cm<sup>3</sup> with rising initial gas pressure, and the  $D_V$  increases from 2.13 to 2.53 accordingly. Compared with the  $D_V$  of samples without gas, the  $D_V$  increased by 10.32%, 17.99%, 26.46%, and 32.80% respectively. In other words, when gas pressure increases, the crack volume and fractal dimension of coal samples rise.

In summary, gas aggravates the splitting-spallation composite failure of coal samples.

### 5 Discussions

The trend of dynamic mechanical parameters, crack volume, and fractal dimension at the mesoscopic level of impacted samples under distinct initial gas pressure are analyzed above. However, the mechanism of gas deteriorated mechanical parameters and aggravated crack propagation of coal samples under the combined dynamic and static loads remains to be revealed.

#### 5.1 Discussion on gas deteriorated mechanical parameter of coal sample

Firstly, the surface energy of GAS can be represented as follows (He et al. 1996):

$$\gamma = \gamma_0 - \frac{RT}{V_0S} \int_0^p \frac{V_p}{p} dp \tag{3}$$

Steverding and Lehnigk (1970, 1976) deduced that the failure condition of materials caused by stress pulses ( $\sigma_i(t)$ ) of arbitrary shape is as follows:

$$\int_0^t \sigma_i^2(t) dt \geq \frac{\pi \gamma E_s}{c_s} \tag{4}$$

It is assumed that an ideal half-periodic sinusoidal stress pulse acting on the material is  $\sigma_d$  (Steverding and Lehnigk 1976; Li 2014), that is:

$$\sigma_i(t) = \sigma_d \sin \frac{2\pi t}{T_i}, \quad 0 \leq t \leq \frac{T_i}{2} \tag{5}$$

Simultaneous Eqs. (4) and (5), the condition for material failure under the action of half-periodic sinusoidal stress pulses is obtained:

$$\sigma_d^2 = \frac{8\pi^2 \gamma E_s}{c_s \left(4\pi t - T_i \sin \frac{4\pi t}{T_i}\right)} \tag{6}$$

The Eq. (3) can be substituted for Eq. (6):

$$\sigma_d^2 = \frac{8\pi^2 \gamma_0 E_s}{c_s \left(4\pi t - T_i \sin \frac{4\pi t}{T_i}\right)} - \frac{8\pi^2 E_s}{c_s \left(4\pi t - T_i \sin \frac{4\pi t}{T_i}\right)} \frac{RT}{V_0S} \int_0^p \frac{V_p}{p} dp \tag{7}$$

In particular, based on Eq. (6), the dynamic strength of gas-free coal ( $\sigma_0$ ) can be represented by the formula given below:

$$\sigma_0^2 = \frac{8\pi^2 \gamma_0 E_s}{c_s \left(4\pi t - T_i \sin \frac{4\pi t}{T_i}\right)} \tag{8}$$

It is assumed that the adsorption curve conforms to the Langmuir equation (Wang et al. 2021b):

$$V_p = \frac{abp}{1 + bp} \tag{9}$$

Simultaneous Eqs. (7) to (9):

$$\left(\frac{\sigma_d}{\sigma_0}\right)^2 = 1 - \frac{aRT}{\gamma_0 V_0 S} \ln(1 + bp) \tag{10}$$

where,  $\gamma_0$  and  $\gamma$  represent the surface energy of gas-free coal and GAS, respectively;  $R$  is the general gas constant;  $T$  is the absolute temperature;  $V_0$  is the molar volume;  $S$  is the specific surface area;  $V_p$  is the amount of gas adsorption at equilibrium adsorption;  $E_s$  is the initial elastic modulus;  $T_i$  is the period of stress pulse;  $a$  is the limit capacity of adsorption at reference pressure;  $b$  is the equilibrium constant for adsorption.

Secondly, according to Bangham hypothesis (Wang et al. 1994), the correlation between strain caused by the gas effect and surface energy of GAS under load constraints is as follows:

$$\Delta \epsilon = \lambda \Delta \gamma \tag{11}$$

In the above formula,  $\Delta \epsilon$  is the expansion strain of GAS under load constraints;  $\lambda$  is a proportional coefficient, whose value can be represented as  $\lambda = 2S\rho_c/9K$ , where  $K$ ,  $\rho_c$  are the bulk modulus and initial apparent density of the coal;  $\Delta \gamma$  represents the change in the surface energy of coal.

Therefore, the failure strain of GAS under the coupled dynamic and static loads is as follows:

$$\epsilon_m^e = \epsilon_m^0 + \Delta \epsilon \tag{12}$$

The model of failure strain of the coal under the gas occurrence can be found by substituting Eqs. (3), (9), and (12) for Eq. (13).

$$\epsilon_m^e = \epsilon_m^0 + \frac{2a\rho_c RT \ln(1 + bp)}{9V_0K} \tag{13}$$

where,  $\epsilon_m^0$  and  $\epsilon_m^e$  are the dynamic failure strain of gas-free coal and GAS under combined dynamic and static loads, respectively.

In summary, it can be obtained from Eqs. (10) and (13) that the coal samples' dynamic strength reduces and the failure strain increases synchronously with rising gas pressure, and the theoretical verification is consistent with the experimental results.

### 5.2 Discussion on gas aggravates failure of coal

Internal cracks in GAS are regarded as ideal ellipses (Muskhelishvili 1955). The gas action is equivalent to the tensile stress acting on a certain value at the crack tip (He et al. 1996; Wang et al. 2021a), combined with the failure mode of impacted coals, therefore, the meso-crack can be regarded as a type I. The effective transverse compressive stress ( $\sigma_o^*$ ) and effective normal compressive stress ( $\sigma_n^*$ ) under gas pressure are obtained:

$$\begin{cases} \sigma_o^* = \frac{(\sigma_1 + \sigma_3) - (\sigma_1 - \sigma_3) \cos 2\alpha}{2} - (p_0 + \Delta p) \\ \sigma_n^* = \frac{(\sigma_1 + \sigma_3) + (\sigma_1 - \sigma_3) \cos 2\alpha}{2} - (p_0 + \Delta p) \end{cases} \quad (14)$$

In the formula,  $\sigma_1$  and  $\sigma_3$  are the maximum and minimum principal stress, respectively;  $p_0$  and  $\Delta p$  are the initial gas pressure and desorption gas pressure, respectively;  $\alpha$  is the angle between the crack and the minimum principal stress.

Then, the stress intensity factor (SIF) of type I of GAS is  $K_I$  (Wang et al. 2021b):

$$K_I = K_{I(o)} + K_{I(n)} = \sqrt{\pi l^*} \left( \sigma_o \sqrt{\frac{r}{l^*}} - \sigma_n \right) = \left[ \frac{(\sigma_1 + \sigma_3) - (\sigma_1 - \sigma_3) \cos 2\alpha}{2} - (p_0 + \Delta p) \right] \sqrt{\pi r} - \left[ \frac{(\sigma_1 + \sigma_3) + (\sigma_1 - \sigma_3) \cos 2\alpha}{2} - (p_0 + \Delta p) \right] \sqrt{\pi l^*} \quad (15)$$

where,  $K_{I(o)}$  and  $K_{I(n)}$  are stress intensity factors caused by tensile stress and normal compressive stress, respectively; in which  $K_{I(o)}$  is established if  $r/l^* \rightarrow 0$ ;  $r$  is the curvature radius at the crack tip;  $l^*$  is the long half axis of the ellipse.

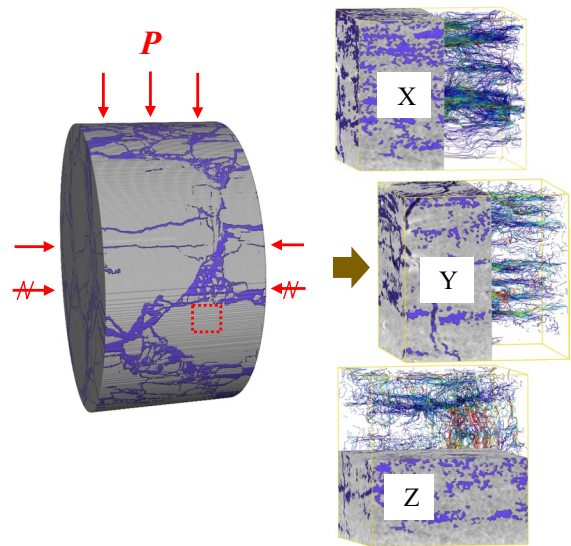


**Fig. 11** Model of gas-bearing coal under dynamic and static combined loading

The stress state of GAS under dynamic and static loads is depicted in Fig. 11. Among them, the left disc represents the force diagram of the gas-bearing coal at the moment of impact,  $P$  represents the gas pressure, the straight-line arrow and the broken-line arrow represent the static load and the dynamic load respectively. The 3cubes on the right side represents the gas flow in the X, Y and Z directions of the micro-element in the coal samples. Based on the above stress state of GAS and the calculation method

of SIF, the SIF of GAS under dynamic and static loads can still be represented by Eq. (15). Among them, the stress of GAS includes the combined force of dynamic and static load (uniformly expressed by  $\sigma_1$ ) and the gas surface force ( $p$ ) acting on the coal's

surface (the gas pore pressure after adsorption equilibrium is equal to the gas pressure outside the coal in the gas sealing device, so the effective confining pressure of coal is 0). Therefore, the SIF of GAS under dynamic and static load is calculated as follows:

$$K_I = K_{I(o)} + K_{I(n)} = \sqrt{\pi l^*} \left( \sigma_o \sqrt{\frac{r}{l^*}} - \sigma_n \right) = \left[ \frac{\sigma_1 - \sigma_1 \cos 2\alpha}{2} - (p_0 + \Delta p) \right] \sqrt{\pi r} - \left[ \frac{\sigma_1 + \sigma_1 \cos 2\alpha}{2} - (p_0 + \Delta p) \right] \sqrt{\pi l^*} \tag{16}$$

Since the condition for  $K_{I(o)}$  to be established is  $r/l^* \rightarrow 0$ , then the Eq. (16) can be transformed into:

$$K_I = K_{I(o)} + K_{I(n)} = \sqrt{\pi l^*} \left( \sigma_o \sqrt{\frac{r}{l^*}} - \sigma_n \right) = \left[ \frac{\sigma_1 - \sigma_1 \cos 2\alpha}{2} - (p_0 + \Delta p) \right] \sqrt{\pi l^*} \sqrt{\frac{r}{l^*}} - \left[ \frac{\sigma_1 + \sigma_1 \cos 2\alpha}{2} - (p_0 + \Delta p) \right] \sqrt{\pi l^*} \tag{17}$$

Therefore:

$$K_I = K_{I(o)} + K_{I(n)} = \left[ (p_0 + \Delta p) - \frac{\sigma_1 + \sigma_1 \cos 2\alpha}{2} \right] \sqrt{\pi l^*} \tag{18}$$

Equation (18) illustrates that the SIF of GAS is strongly associated with the initial gas pressure, external load, crack length, and the angle between the long axis and the horizontal direction. In addition, the SIF of type I crack rises with the rise of initial gas pressure and desorption gas pressure. The studies show that when the SIF of type I crack increases fracture toughness ( $K_I$ , it is the property and has nothing to do with the external stress state), it leads to the increase of stress near the crack tip and promotes rapid propagation of cracks. Therefore, gas aggravates the compound failure of GAS.

### 6 Conclusion

Utilizing a self-developed observable combined dynamic and static loading test system of GAS, the dynamic compression experimentation of coal samples was carried out. The mechanical properties including the coal samples' failure mode during distinct initial gas pressures were studied. Moreover, the

mechanism of gas deteriorated mechanical parameters and aggravated propagation of cracks during the combined dynamic and static loads revealed. The results indicated the following conclusions:

- (1) The gas tightness criterion and one-dimensional stress wave hypothesis are both satisfied by the observable combined dynamic and static loading

- test system of GAS, which can successfully conduct dynamic experiments and real-time recording of the GAS failure process.
- (2) There is no evident compaction stage on the dynamic stress-strain curve for GAS, which is separated into four stages: linear elastic stage, elastoplastic stage, plastic stage, and failure stage. The coal samples' average dynamic strength and failure strain deteriorate with the rise of initial gas pressure, and the maximum deterioration degree values compared to that under no gas pressure are 36.91% and 17.65%, respectively. Additionally, compared to the static strength, the dynamic strength had more gas sensitivity.
- (3) Based on CT technology, it is found that the splitting-spallation composite cracks of impacted coal samples become more prominent with rising initial gas pressure, and finally, the two kinds of cracks create a complex reticular crack system. In addition, the crack propagation degree under different initial gas pressure was quantitatively analyzed using the fractal theory. The crack volume and fractal dimension increase with rising gas pressure, indicating that gas can aggravate the failure degree of coal.
- (4) Through theoretical analysis, the deterioration model of mechanical parameters of GAS under combined dynamic and static loading is obtained,

that is, with increasing gas pressure, the coal samples' dynamic strength decreases and the failure strain rises synchronously, which is confirmed by the experimental results. Meanwhile, the primary cause for the aggravation of coal compound failure is that the stress intensity factor of type *I* crack rises with the rise of initial gas pressure and desorption gas pressure.

**Acknowledgements** This work was financially supported by the Collaborative Innovation Funding Project of Anhui Universities (No. GXXT-2020-055).

**Author contributions** HL: Conducting a research and analysis; LW: Conceptualization and funding acquisition; HZ: Reviewing; SL: Preparing material.

**Data availability** The related data used to support the findings of this study are included within the article.

#### Declarations

**Ethics approval and consent to participate** Not applicable.

**Consent for publication** The authors agree with the publication of the manuscript.

**Competing interests** The authors declare that we have no known competing financial interests or personal relationships that could have appeared to influence the work reported in this paper.

**Open Access** This article is licensed under a Creative Commons Attribution 4.0 International License, which permits use, sharing, adaptation, distribution and reproduction in any medium or format, as long as you give appropriate credit to the original author(s) and the source, provide a link to the Creative Commons licence, and indicate if changes were made. The images or other third party material in this article are included in the article's Creative Commons licence, unless indicated otherwise in a credit line to the material. If material is not included in the article's Creative Commons licence and your intended use is not permitted by statutory regulation or exceeds the permitted use, you will need to obtain permission directly from the copyright holder. To view a copy of this licence, visit <http://creativecommons.org/licenses/by/4.0/>.

#### References

- Ai D, Zhao Y, Wang Q, Li C (2019) Experimental and numerical investigation of crack propagation and dynamic properties of rock in SHPB indirect tension test. *Int J Impact Eng* 126:135–146
- Ates Y, Barron K (1988) The effect of gas sorption on the strength of coal. *Min Sci Technol* 6(3):291–300
- Barile C, Casavola C, Pappalettera G, Vimalathithan PK (2019) Damage characterization in composite materials using acoustic emission signal-based and parameter-based data. *Compos B Eng* 178:107469
- Bieniawski ZT (1968) The effect of specimen size on compressive strength of coal. *Int J Rock Mech Min Sci Geomech* 5(4):325–335
- Chen YS, Li N, Han X, Pu YB, Liao QR (2005) Research on crack developing process of non-interpenetrated crack media by using CT. *Chin J Rock Mech Eng* 24(15):2665–2670
- Fu YK, Xie BJ, Wang QF (2013) Dynamic mechanical constitutive model of the coal. *J China Coal Soc* 38(10):1769–1774
- Fu Y, Chen X, Feng ZL (2020) Characteristics of coal-rock fractures based on CT scanning and its influence on failure modes. *J China Coal Soc* 45(2):568–578
- Ge XR, Ren JX, Pu YB, Ma W, Zhu YL (1999) A real in time CT triaxial testing study of meso-damage evolution law of coal. *Chin J Rock Mech Eng* 18(5):497–502
- Han ZY, Li DY, Zhou T, Zhu QQ, Ranjith PG (2020) Experimental study of stress wave propagation and energy characteristics across rock specimens containing cemented mortar joint with various thicknesses. *Int J Rock Mech Min Sci* 131:104352
- Hao Y, Hao H, Zhang XH (2012) Numerical analysis of concrete material properties at high strain rate under direct tension. *Int J Impact Eng* 39(1):51–62
- Hao XJ, Du WS, Zhao YX, Sun ZW, Zhang Q, Wang SH, Qiao HQ (2020) Dynamic tensile behaviour and crack propagation of coal under coupled static-dynamic loading. *Int J Min Sci Technol* 30(5):659–668
- He XQ, Wang EY, Lin HY (1996) Coal deformation and fracture mechanism under pore gas action. *J China Univ Min Technol* 25(1):6–11
- Jiao ZH, Mu CM, Wang L, Cui ZL, Yuan QP, Zou P, Wang J (2021) Tests for dynamic mechanical properties of coal impact compression under passive confining pressure. *J Vib Shock* 40(21):185–193
- Jin JF, Li XB, Yin ZQ, Zou Y (2011) A method for defining rock damage variable by wave impedance under cyclic impact loadings. *Rock and Soil Mechanics* 32(05):1385–1393
- Klepaczko JR, Hsu TR, Bassim MN (1984) Elastic and pseudoviscous properties of coal under quasi-static and impact loadings. *Can Geotech J* 21(2):203–212
- Kong XG, Wang EY, Li SG, Hu SB, Li JD (2020) Dynamics characteristics of gas-bearing coal under shock load. *J China Coal Soc* 45(3):1099–1107
- Kong X, Li S, Wang E, Ji P, Wang X, Shuang H, Zhou Y (2021) Dynamics behaviour of gas-bearing coal subjected to SHPB tests. *Compos Struct* 256:113088
- Lemaitre J (1984) How to use damage mechanics. *Nuclear Eng Des J* 80(2):233–245
- Li XB (2014) *Rock dynamics fundamentals and applications*. Science Press, Beijing
- Li XB, Zuo YJ, Ma CD (2005) Failure criterion of strain energy density and catastrophe theory analysis of rock subjected to

- static-dynamic coupling loading. *Chin J Rock Mech Eng* 24(16):2814–2824
- Li XB, Zhou ZL, Lok TS, Hong L, Yin TB (2008) Innovative testing technique of rock subjected to coupled static and dynamic loads. *Int J Rock Mech Min Sci* 45(5):739–748
- Li ZW, Hao ZY, Pang Y, Gao YB (2015) Fractal dimensions of coal and their influence on methane adsorption. *Int J Coal Geol* 40(04):863–869
- Liu BX, Huang JL, Wang ZY, Liu L (2009) Study on damage evolution and acoustic emission character of coal-rock under uniaxial compression. *Chin J Rock Mech Eng* 28(S1):3234–3238
- Liu JH, Zhou YC, Yang HT, Fu SF, Gu Y (2019) Energy and damage characteristics of shaft lining concrete subjected to impact. *J China Coal Soc* 44(10):2983–2989
- Liu HQ, Wang L, Xie GX, Yuan QP, Zhu CQ, Jiao ZH (2022) Comprehensive characterization and full pore size fractal characteristics of coal pore structure. *J Min Saf Eng* 39(3):458–479
- Liu HQ, Wang L, Xie GX (2023) Dynamic compression behavior of coal under different initial gas pressures. *Rock Mech Rock Eng* 56:2213–2228
- Lu FY, Chen R, Lin YL, Zhao PZ, Zhang D (2013) Hopkinson bar techniques. Science Press, Beijing
- Ma DP, Zhou Y, Liu CX, Shang YD (2019) Energy evolution characteristics of coal failure in triaxial tests under different unloading confining pressure rates. *Rock Soil Mech* 40(07):2645–2652
- Ma Q, Tan YL, Liu XS, Gu QH, Li XB (2020) Effect of coal thicknesses on energy evolution characteristics of roof rock-coal-floor rock sandwich composite structure and its damage constitutive model. *Compos B Eng* 198:108086
- Medhurst TP (1997) Estimation of the in situ strength and deformability of coal for engineering design. Brisbane: The University of Queensland School of Engineering
- Muskhelishvili NI (1955) Some basic problems of the mathematical theory of elasticity. *Am Math Monthly*
- Ranjith PG, Jasinge D, Choi SK, Mehic M, Shannon B (2010) The effect of CO<sub>2</sub> saturation on mechanical properties of Australian black coal using acoustic emission. *Fuel* 89(8):2110–2117
- Steverding B, Lehnigk SH (1970) Response of cracks to impact. *J Appl Phys* 41:2096–2099
- Steverding B, Lehnigk SH (1976) The fracture penetration depth of stress pulses. *Int J Rock Mech Min Sci* 13:75–80
- Technical specification for testing method of rock dynamic properties: T/CSRME 001-2019. Beijing: Chinese Society for Rock Mechanics and Engineering.
- Thararoop P, Karpyn ZT, Ertekin T (2012) Development of a multi-mechanistic, dual-porosity, dual-permeability, numerical flow model for coalbed methane reservoirs. *J Nat Gas Sci Eng* 8:121–131
- Viete DR, Ranjith PG (2006) The effect of CO<sub>2</sub> on the geomechanical and permeability behaviour of brown coal: Implications for coal seam CO<sub>2</sub> sequestration. *Int J Coal Geol* 66(3):204–216
- Wang Y, Wu J, Yang S (1994) Prevention and administration of coal mining gas. China Coal Industry Publishing House, Beijing
- Wang C, Chen W, Hao H, Zhang S, Song R, Wang X (2018) Experimental investigations of dynamic compressive properties of roller compacted concrete (RCC). *Constr Build Mater* 168:671–682
- Wang DK, Zhang H, Wei JP, Wu Y, Zhang HT, Yao BH, Fu JH, Zhao LZ (2021a) Dynamic evolution characteristics of fractures in gas-bearing coal under the influence of gas pressure using industrial CT scanning technology. *J China Coal Soc* 46(11):3550–3564
- Wang L, Liu HQ, Xie GX, Yuan QP, Chen LP (2021b) Fine characterization of the pore and fracture structure and strength degradation mechanism of gas bearing coal. *Rock and Soil Mechanics* 42(12):3203–3216
- Wang L, Yuan QP, Xie GX et al (2022) Length-diameter ratio effect of energy dissipation and fractals of coal samples under impact loading. *J China Coal S* 47(4):1534–1546
- Xie GX, Hu ZX, Wang L (2014) The coupling effect of the coal seam gas pressure and mining stress in working face. *J China Coal Soc* 39(6):1089–1093
- Xie GX, Yin ZQ, Hu ZX, Hou JL, Ma HF (2015) Disaster-causing mechanical mechanism of coal mining dilatancy of gassy seam in deep mine. *J China Coal Soc* 40(1):24–29
- Xie GX, Yin ZQ, Wang L, Hu ZX, Zhu CQ (2017) Effects of gas pressure on the failure characteristics of coal. *Rock Mech Rock Eng* 50(7):1711–1723
- Xu JY, Lu XC, Zhang J, Wang ZD, Bai EL (2010) Research on energy properties of rock cyclical impact damage under confining pressure. *Chin J Rock Mech Eng* 29(S2):4159–4165
- Yang K, Wei Z, Dou LT, Chi XL, Liu WJ, Zhang JQ (2021) Research on dynamic tensile energy evolution and fractal characteristics of water-bearing coal samples. *J China Coal Soc* 46(2):398–411
- Yin Z, Chen W, Hao H, Chang J, Zhao G, Chen Z, Peng G (2020) Dynamic compressive test of gas-containing coal using a modified split hopkinson pressure bar system. *Rock Mech Rock Eng* 53(2):815–829
- Yuan L (2021) Research progress of mining response and disaster prevention and control in deep coal mines. *J China Coal Soc* 46(03):716–725
- Yuan QP, Xie GX, Wang L, Jiao ZH, Zou P, Liu HQ, Khan NM (2021) Experimental study on stress uniformity and deformation behavior of coals with different length-to-diameter ratios under dynamic compression. *Shock Vib* 2021:1–12
- Zhang WQ, Mu CM, Li ZQ (2019) Study on dynamic mechanical properties of coal under impact loading. *Coal Sci Technol* 47(10):198–204
- Zhao CX, Li YM, Liu G, Meng XR (2020) Mechanism analysis and control technology of surrounding rock failure in deep soft rock roadway. *Eng Fail Anal* 115:104611